International Journal of Heat and Fluid Flow 78 (2019) 108437

Contents lists available at ScienceDirect

International Journal of Heat and Fluid Flow

journal homepage: www.elsevier.com/locate/ijhff

Gas–liquid slug flow in a horizontal concentric annulus, a comparison of numerical simulations and experimental data

C. Friedemann[*,a], M. Mortensen[a], J. Nossen[b]

[a] Department of Mathematics University of Oslo, Moltke Moes vei 35, OSLO 0851, Norway
[b] Institute for Energy Technology, Kjeller, 2007, Norway

ARTICLE INFO

Keywords:
Annulus
Slug flow
Volume of fluid
Reynolds-averaged Navier–Stokes equations

ABSTRACT

Multiphase flow simulations were run in OpenFOAM utilizing InterFoam, a volume of fluid type solver. A concentric annulus geometry was constructed and periodic boundary conditions were applied to alleviate the requirement for a longer domain. The simulations were run in 3, 5 and 7 m long domains with the annulus dimensioned such that the outer and inner cylinder diameter were 0.1 and 0.05 m respectively. The 4 individual mesh designs were constructed such that the coarsest mesh consists of 102k cells/m while the finest mesh was generated with 400k cells/m. Each mesh was significantly refined within 0.005 m of both the inner and outer cylinder wall. The simulation data was compared with experimental pressure and holdup data collected at Institute for Energy Technology in Norway. The 3 and 7 m domains reproduced slug frequencies to within 9% of the experiment results of 1.43 Hz for all mesh densities. Comparatively, the 5 m domain has larger errors with respect to slugging frequency (22–27%). The 5 m case performs poorly, probably due to an artificial restraint introduced by the limitation of available liquid which is set as $\alpha_{oil} = 0.53$ for all cases. The α_{oil} restriction combined with the domain length determines the amount of liquid in the system. This interaction of factors means that the domain length is an important parameter when preparing the simulation. The pressure data display a stronger dependence on the mesh quality in comparison to the slug frequency analysis. The 3 m domain with a 400k cells/m mesh resulted in a maximum and minimum pressure gradient of 1783.5 and 803.9 Pa/m, compared to the experiment values of 1785 and 822 Pa/m, which are within 3% of the expected results.

1. Introduction

During the spring of 2010 a catastrophic event at the Macondo prospect in the Gulf of Mexico devastated the United States coastline and ocean ecosystem. The Macondo accident was compounded when the annular blowout preventer failed (LP, 2014; BP, 2010; Transocean, 2011). Following the system failure leakage through the annulus caused several hundred million liters of oil to seep into the ocean before the rupture was eventually sealed.

The ability to predict the outlet phase fractions as well as flow rates is imperative when estimating the scope of disasters caused by an uncontrolled release of environmentally harmful hydrocarbons. As noted by Gidaspow et al. (2013), there are doubts related to whether the models employed by BP in the aftermath of the oil spill were accurate. The uncertainty related to the scope of the disaster underlines the importance of understanding the annulus flow problem. The issue is further emphasized when accounting for the current status and delicate balance of our environment and ecosystem.

The modeling, simulation and validation of two-phase pipe-flow and flow regimes are fairly well understood. We can conduct reasonably accurate simulations of pressure drop, as well as reproduce flow regimes and holdup profiles from experiments (Issa and Kempf, 2003; Knotek, 2014; Valle et al., 2008; Housz et al., 2017; Parsi et al., 2017). Compared to conventional pipe flow, the special case of the annulus configuration with a submerged internal cylinder interfering with the surrounding flow is significantly less studied. There are very few if any CFD simulations which are validated by experiments. As such this paper will present simulations of a specific case based on data gathered during experiments at the Institute for Energy Technology (IFE) in Norway, the results from which have been made available as part of this project.

There are several cases of intended annulus flow within the oil and gas industry. The geometry exists between the drill pipe and casing during drilling, in a gas lifted well, and in some special cases between the tubing and casing. Although the Macondo incident and indeed most

* Corresponding author.
E-mail address: chrisjfr@student.matnat.uio.no (C. Friedemann).
URL: https://www.mn.uio.no/math/personer/vit/chrisjfr/ (C. Friedemann).

https://doi.org/10.1016/j.ijheatfluidflow.2019.108437
Received 14 December 2018; Received in revised form 25 June 2019; Accepted 1 July 2019
Available online 06 July 2019

applications of the annulus configuration occurs in a vertical orientation, there are relevant annulus applications related to a horizontal orientation, such as multi-stage horizontal fracking systems (Bellarby et al., 2013). The combination of intended and unintended occurrences of annulus flow and the aftereffects of a system failure warrants the need for extensive research into understanding and predicting the behavior of multiphase flow within an annulus.

Reviewing the annulus flow body of work, we realize that there lacks literature compared to other configurations. Beyond the experimental tests and early work on annulus flow done by Kelessidis and Dukler related to vertical, concentric and eccentric annuli (Kelessidis and Dukler, 1989) from 1989, as well as Caetano's (Caetano, 1985) 1992 thesis there is scarce research covering the topic. We can identify a small body of work that deals with horizontal annuli (Sorgun et al., 2013; Ekberg et al., 1999; Chung and Sung, 2003) as well as vertical (Hasan and Kabir, 1992; Julia and Hibiki, 2011; Julia et al., 2011; Jeong et al., 2008), inclined (Hasan and Kabir, 1992; Wongwises and Pipathattakul, 2006), coiled (Xin et al., 1997), rotating (Hadžiabdić et al., 2013; Chung and Sung, 2005) and obstructed annuli (Bicalho et al., 2016). The majority of which are experimental, of considerable age and in some cases single phase. Additionally, the literature rarely addresses slug flow. Finally, most of the existing work is based on the concentric annulus configuration. The eccentricity of the annulus has an effect on the wetted surface area and frictional forces, which in turn alters pressure drop and turbulence generation. Considering this, it stands to reason that the eccentricity of the annulus should be a parameter given additional attention in later works along with other parameters such as viscosity.

Concurrent with the constant advances related to computing power, computational methods and CFD code efficiency, it has become realistic to conduct numerical simulations of several types of complex multiphase pipe flow. Among these are geometries such as T-junction risers (Tunstall and Skillen, 2016), wavy pipe (Xing et al., 2013), ventilated vertical pipe (Xiang et al., 2011), horizontal loop (Hossain et al., 2011) and even single phase flow in an annulus with a rotating inner (Chung and Sung, 2005; Escudier et al., 2000) or outer (Hadžiabdić et al., 2013) cylinder. In conjunction with the ability to simulate intricate geometries, similar advances were made with complex flows. Complex flows in the form of droplets (Verdin et al., 2014), slurry (Zambrano et al., 2017), bubbly flow (Rzehak and Kriebitzsch, 2015; Rzehak and Krepper, 2013; Colombo and Fairweather, 2015), three-phase in a U-bend (Pietrzak and Witczak, 2013) and slug flow (Hua et al., 2014; Shuard et al., 2016) are all flows that are possible to resolve within a reasonable amount of time.

All of these more or less new developments point toward the viability of conducting realistic CFD simulations of slug flow within an annulus configuration. Even though the annulus configuration in itself is a simple geometry, complexity is introduced through the internal pipes interaction with the flow. The inner pipe has the effect of increasing the overall interfacial area between wall and fluid while decreasing the interfacial area between the two fluids. Consequently, when the inner pipe is fully concentric, that is to say that the distance between the inner and outer pipe is constant, the friction factor is increased. Alternatively, for a fully eccentric pipe the opposite is true, the friction factor will always be lower than that of a regular pipe (Caetano, 1985). Therefore, depending on the eccentricity of the annulus we can expect to see markedly different behavior such as altered pressure drop, flow regimes and turbulence generation. Considering the pronounced impact of eccentricity, the annulus eccentricity is seen as an ideal topic for future work.

In this paper we have studied a specific concentric case, and compared the numerical results with available experimental data from IFE. The fluid density, viscosity and flow rates are dictated by the experimental set up and mimicked in the simulation cases. The collected experiment data represents a typical slug flow, which is defined by a body of liquid which periodically bridges the entire cross section. Although the topic of this paper is slug flow, in the future we expect to be able to develop flow regime maps akin to those created for conventional pipe flow. By analyzing diverse cases from several campaigns, including wavy flow and dispersed bubbly flow, it will be possible to compare the simulations with mechanistic models such as those by Taitel and Dukler (1976), flow regime maps and correlations.

The simulations were run with a fully concentric annulus and periodic boundary conditions. Periodic boundary conditions were chosen in an attempt to alleviate the need for a much longer domain. The natural step in order to simulate a slug flow would be to construct a domain long enough to support several simultaneous slugs. Periodic boundary conditions circumvent this requirement by having a pseudo infinite pipe. The drawback is that there is limited room for redistribution of the liquid within the system, which in turn restricts the number of possible simultaneous slugs.

The pipe lengths studied were 3, 5 and 7 m. The pipe lengths were chosen to analyze the effect of the domain length on the solution. The Reynolds-averaged Navier–Stokes (RANS) implementation of the InterFoam solver within the OpenFOAM framework was used to run the simulations. The InterFoam solver which employs the volume of fluid (VOF) method has been shown to be applicable to a variety of complex flows such as jets (Deshpande et al., 2012), slug and annular flow (Shuard et al., 2016), droplets (Dianat et al., 2017) and t-junction risers (Tunstall and Skillen, 2016). The holdup profile and pressure gradient in particular will be compared with the experimental data collected at IFE.

2. Model

2.1. Geometry and mesh

The computational domain consists of a concentric annulus with an outer cylinder diameter (O.D) of 0.1 m, while the inner cylinder has a diameter (I.D) of 0.05 m. As mentioned, the 3 different domain lengths were used to investigate the effects of the amount of available liquid and number of slugs within the domain on the pressure gradient and liquid holdup profile.

Varying mesh densities were utilized to study the effect of the resolution on the solution. The coarsest mesh was designed with 108k cells/m while the finest mesh consisted of 400k cells/m. A comparison of the cross section of the extra coarse, very coarse, medium and very fine mesh are presented in Fig. 1.

The meshes shown in Fig. 1 and summarized in Table 1 were constructed in Gmsh and consist of two main regions, the near wall and the interior. Each cell expanding out from either cylinder grow thicker as they approach the constant cell thickness maintained within the rinterior area. The near wall cells are significantly refined in order to more accurately describe the flow in these regions. The shear flow which occurs close to the wall due to the no slip condition contributes to the instability of the interface and is therefore crucial to the overall flow development. The model utilizes a symmetry condition across the y-axis, which effectively halves the cell count. When combined with the

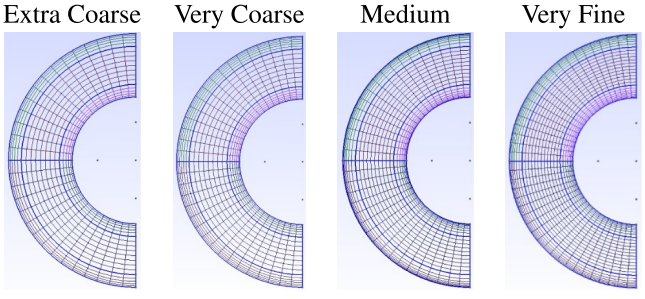

Fig. 1. Side by side comparison of increasing mesh density. Ref. Table 1.

Table 1
Mesh information.

Mesh	Circumference cells	Interior cells	Cells/m
E.Coarse	30	18	$102 \cdot 10^3$
V.Coarse	34	20	$150 \cdot 10^3$
Medium	36	24	$200 \cdot 10^3$
V.Fine	42	26	$400 \cdot 10^3$

utilized RANS model, the symmetry condition results in negligible loss of accuracy (Shuard et al., 2016).

The mesh information displayed in Table 1 summarizes the number of cells per meter, as well as along the circumference and within the interior region of each mesh. The mesh is built by placing hexahedral elements along transfinite lines. Transfinite lines are lines used to distribute the elements according to a chosen progression. There are transfinite lines placed along the circumference, along which the cells are evenly distributed. Additionally, there are transfinite lines connecting the inner and outer cylinder. Within the wall region a progression of 1.2 is applied, thus each cell is 20% larger than the preceding cell. Within the central interior region a constant cell sizing is employed. By carefully distributing the number of nodes along each transfinite line, the mesh sizing and element type can be controlled. This procedure ensures the exact placement of elements, thereby guaranteeing a precise match between the inlet and outlet.

The match between the inlet and outlet patches is important for any OpenFoam simulation using periodic boundary conditions. A poor match between two connecting patches such as the inlet and outlet can result in an alteration of the flow field during patch transfer.

3. Numerical method

The solver employed in this set of simulations was as previously mentioned the interFoam solver within OpenFoam. Although interFoam accepts a variety of turbulence models, these simulations used the k-ω RANS model in combination with periodic boundary conditions. The turbulence model solves for the kinetic energy (k) and specific dissipation rate (ω) by use of partial differential equations.

The InterFoam solver treats the mixture of the two fluids as a single imaginary fluid. In order to do so it applies mixture rules to determine the mixture velocity ($\bar{u}$), density ($\bar{\rho}$) and viscosity ($\bar{\nu}$). The mixture rule utilized in the InterFoam framework is described in Eq. (1). The average mixture velocity is determined as a function of the gas (u_g) and liquid (u_l) velocity, as well as the respective phase fractions (α_g, α_l).

$$\bar{u} = \alpha_g u_g + \alpha_l u_l, \tag{1}$$

the average mixture density and viscosity is solved by applying the same procedure.

If we consider the two fluids incompressible and apply the averaging procedure described in Eq. (1) to the fundamental conservation of continuity and momentum equations, the continuity equation can be simplified as

$$\nabla \cdot \bar{u} = 0, \tag{2}$$

and the corresponding momentum equation becomes

$$\frac{\partial \bar{u}}{\partial t} + \nabla \cdot (\bar{u}\bar{u}) = -\frac{1}{\bar{\rho}} \nabla p + \nabla \cdot (\bar{\nu}(\nabla \bar{u} + (\nabla \bar{u})^T)) + g + \frac{F_s}{\bar{\rho}}. \tag{3}$$

The terms p,g, and F_s denote pressure, gravity, and surface tension force respectively. A more comprehensive derivation and description of the solver can be studied in Lopes (2013).

By treating the two fluids as a single imaginary fluid, using Eqs. (2) & (3) the solver resolves the equations once for each iteration instead of repeating them for each phase. In order to keep track of the position and interface between the phases an indicator function, Eq. (4) is used in combination with an advection function Eq. (5) to predict the transport of the phase fluids. In general form, as described in Khalili et al. (2016) the indicator function (γ) is summarized as

$$\gamma = \begin{cases} 1 & \text{if cell is occupied by phase 1} \\ 0 < \gamma < 1 & \text{if phase 1 and phase 2 interfaces} \\ 0 & \text{if cell is occupied by phase 2,} \end{cases} \tag{4}$$

and the advection function takes the form of

$$\frac{\partial \gamma}{\partial t} + \nabla \cdot (\gamma \bar{u}) + \nabla \cdot (u_c \gamma (1 - \gamma)) = 0. \tag{5}$$

The last term on the L.H.S is an added term used to help with the conservation of phases by reducing numerical diffusion, which can cause smearing of the interface. Smearing is known to be a potential problem with VOF type solvers and can contribute to potential inaccuracy of the solution (Ubbink, 1997; So et al., 2011).

The term u_c, is an artificial interface compression velocity represented as a vector of the relative velocity of the two phases. The general form of the equation used to solve for interface compression velocity was suggested by Weller (2008) and is calculated as

$$u_c = min[C_\gamma |\bar{u}|, max(|\bar{u}|)] \frac{\nabla \gamma}{|\nabla \gamma|}. \tag{6}$$

As described in Berberovic (2010), the interface compression velocity is based on the maximum velocity within the interfacial area. The interface compression (C_γ) is a set constant, and in the case of this work it has been set at 0.8. The constant can theoretically take any value, values above 1 are considered enhanced compression, while a value of 0 is no compression, setting the value to 0 would as a result negate the term completely.

As a benefit of applying periodic boundary conditions, the values of the turbulent kinetic energy (k), specific dissipation (ω) and the initial flow field are only of importance at startup. As the simulation progresses, the values are continuously numerically solved. and updated to reflect the current flow. Therefore, only the initial phase fractions, viscosity and density are of significance to the reader, these are summarized in Table 2.

The surface tension (σ) which was measured during the experiment campaign and applied to the simulations was 0.0285 N/m. There was no initial pressure gradient or wave formations prescribed within the initial field. Instead an average mixture flow velocity of 3.6 m/s extracted from the experiment data was used as the periodic flow condition. The simulations are initialized as a stratified smooth flow, as such the pressure gradient and holdup profile undergo a transient at startup while the flow develops. The transient is caused by the sudden formation of a large slug that is not described by the initial conditions.

4. Simulations and results

The simulation cases presented in this paper were based on the holdup and velocity data obtained at IFE during their experiment campaign. The experimental setup at IFE includes 5 differential pressure transducers (DPT) distributed along the top of the annulus test section with an accuracy of ± 6 Pa, and an effective acquisition rate of 1.20 Hz. The 5th set is placed 36 and 39 m downstream of the phase inlets. The data collected at this test location is used as the basis for this work. In addition to the DPT there are 3 broad-beam gamma

Table 2
Fluid properties.

	Oil	Gas	Mixture	Units
α	0.53	0.47	1.0	
ν	$2.0 \cdot 10^{-6}$	$7.56 \cdot 10^{-7}$	$1.415 \cdot 10^{-6}$	$\frac{m^2}{s}$
ρ	801.0	23.82	–	$\frac{kg}{m^3}$

densitometers (GD) and 4 high speed cameras (HSC). The GD and HSC are used in order to acquire holdup data (GD) and aid with flow visualizations (HSC). The flow rates of the two phases are controlled at the inlet section. The data collected during the experiments serves as an excellent point of comparison for the annulus configuration simulations.

The simulation series were run using 4 different mesh densities and 3 pipe lengths. Periodic boundary conditions in combination with the chosen pipe lengths and mesh densities were utilized to study the effect of domain length and mesh density on the flow.

From the slug unit lengths observed in the experiments, a 7 m pipe should be able to produce two simultaneous slugs. Meanwhile, the 5 m pipe has more than sufficient liquid to support one slug while lacking the required liquid to produce two concurrent slugs. Lastly, the 3 m pipe has just enough liquid to support a single slug, which should result in a strong concentration of the slug frequency. Following this suggestion, both the 7 m pipe and 3 m pipe are expected to be an accurate representation of the experimental setup. Conversely, the 5 m domain should produce slugs at a lower frequency, due to restraints imposed on the system by the initial conditions in the form of available liquid. The tendency of domain size to have a direct impact on the flow when applied with periodic boundary conditions was also identified in Frank's work on air-water slug flow (Frank, 2005). Utilizing these domains and mesh densities, the effect of the number of slugs within the domain as well as the pressure gradient required to drive the flow were studied and compared with the experiments.

Due to the rapid growth of computational requirements tied to domain size, it is unrealistic to utilize all meshes for the 7 m domain. Therefore, the 7 m domain is restricted to the two coarsest meshes, while the shorter domains are run with all 4 mesh densities. To illustrate the time scaling associated with the grid sizing, the 5 m 400k cells/m mesh took 5 months to simulate a 30 s window on 20 cores, equivalent to roughly 75,000 CPU hours, while the coarsest mesh simulation lasted a mere 7 days for the same domain length.

4.1. Simulation and experiment phase distribution results

The holdup data collected at IFE was processed by their team using data from the gamma densitometers. As a result of the gas entrapment within the slugs, the liquid holdup will rarely indicate 100%. Caetano (1985) found that in an annulus configuration when a slug arises there are regions where the gas phase passes through the liquid, which is consistent with the collected data. As shown in Fig. 3, the fractional liquid holdup never reaches 1.0, instead it reaches a maximum of around 0.87.

A separate matter is that of small Taylor bubbles separating slugs, and also that of gas pockets entrapped within the liquid layer. A short Taylor bubble as seen in Fig. 2 can separate two slugs. It is important that these occurrences are correctly captured in the analysis. In the simulations the occurrence of large entrapped bubbles (Fig. 8) is a more immediate concern with regards to false positives. In the raw data, these phenomena look similar because the gamma densitometers measure the cross-sectional average holdups. However, it is imperative to distinguish the two because their effect on the flow is different. Two high holdup regions separated by a Taylor bubble should be interpreted as two separate slugs, while occurrences with smaller entrapped bubbles are counted as a single slug. Therefore, a combination of visual confirmation and statistics are used when determining slug frequency.

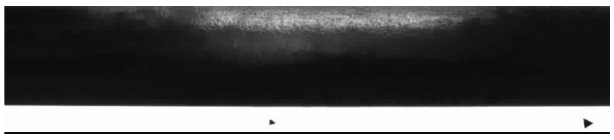

Fig. 2. Two slugs separated by a Taylor bubble.

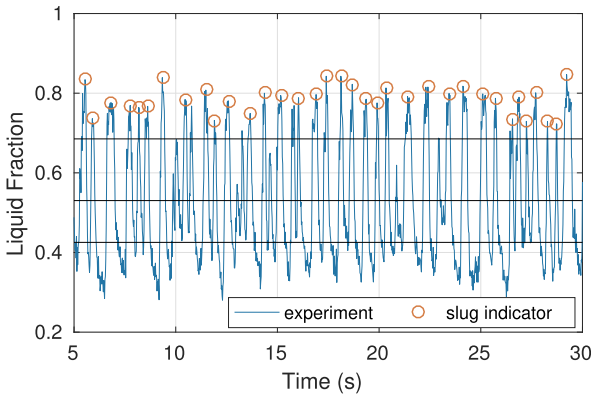

Fig. 3. IFE experiment holdup data, with slug indicators.

Fig. 2 shows a short Taylor bubble with a slug on either side. The image was captured at the 3rd camera location 37m downstream of the inlet. The HSC is placed between the DPT used to measure the pressure gradient. Short Taylor bubbles as shown in Fig. 2 will cause problems for a time based slug filter without careful attention to the parameters. The process used in this paper and by Nuland (1999) is more robust and effective at capturing such phenomena.

The original holdup data (Fig. 3) was processed using a statistical approach (Fig. 4) and visual confirmation. The same procedure was applied to the simulation data. The histograms and labeled slugs were compared with the visual data to ensure that they are consistent with regards to slug frequency. Note that the analysis was run on the full 100 s data set collected in experiment, while only 25 s are presented here for illustration purposes.

By applying filters to the data represented in Fig. 3 we can determine the number of slugs in the sample and the slug frequency. The filtering process follows the procedure described in Nuland's paper on slug analysis (Nuland, 1999). Two thresholds are determined along with the mean holdup. The thresholds are indicated by horizontal lines in Fig. 3. The mean holdup is determined as the average holdup of the time series at the sample point. In this experiment it was determined to be 0.53. The liquid fraction as well as average mixture velocity (3.6 m/s) was used as a basis for the subsequent simulations.

The two conditional holdups are determined using the mean holdup as the starting point. We isolate the data above and below the mean. Among the data points above the mean a conditional holdup is identified as the threshold which identifies a likely slug. For the simulation data, the slug thresholds are generally determined to be in the region of 70% liquid holdup.

Similarly, the data below the mean are used to determine the threshold for the bubble which separates slugs, this threshold is in the region around 40% liquid holdup. The indicator function for slugs will

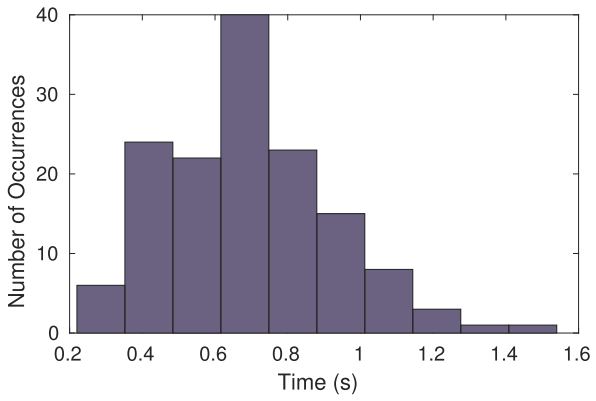

Fig. 4. Histogram of slug distribution from experiment.

only trigger for a new slug if the conditions for slug-bubble-slug transition has been met. Therefore, a new slug is only recognized if the holdup has gone from above the upper threshold, to below the lower threshold and back up again. The filtering process indicates the peak of each identified slug as shown in Fig. 3. The method ensures that there is no inherent time-based filter built into the slug detection, and it relies solely on meeting the necessary conditions as described. The method should detect the occurrence of small Taylor bubbles (Fig. 2) separating two slugs and correctly count them, at the same time it is unlikely that large waves will trigger the indicator function.

By applying the Nuland procedure to the raw data (Fig. 3), we can analyze the data using statistical principles to calculate the mean time interval and standard of the isolated slugs. As shown in Fig. 3, the period between slugs lies within a range of 0.2 to 1.5 s. The majority of them appear in the interval between 0.5 and 1.0 s. The calculated sample mean is 0.697 s (1.43 Hz) and the standard deviation is 0.2302 s. The statistical data matches well with the 20 s visual data captured by the high speed cameras. By applying the same methods used to analyze the experimental data to process the fractional liquid data of the 7 m domain represented in Fig. 5, we can determine the number of slug occurrences. The data analysis results in the identification of 33 slug formations within the 25 second time window of the developed flow field for both meshes. The slug frequency of 1.32 Hz indicates a match with the experimental data to within 10%. We will subsequently notice that the frequency is slightly lower than that observed in the 3 m domain (Fig. 12), and slightly higher than that which occurred in the 5 m domain (Fig. 10) for the same mesh densities.

The maximum holdup of 93.75% for the 102k cells/m mesh and near 99% for the 150k cells/m mesh is higher than that identified during the experiments. Most likely this is a side effect of mesh density and thereby an inability to resolve the small bubbles which permeate through the liquid layer in the experiments. Instead, there is a tendency for large bubbles to form either within the liquid subsequent to wave breaking (Fig. 8), or along the top wall separating the liquid from the wall (Fig. 9).

When we compare the histograms of the 7 m domain (Fig. 6) with the experimental results (Fig. 4), we notice that the bulk of the slug periods (Fig. 6) are concentrated in a span between 0.6 and 0.8 s for the 102k cells/m mesh.

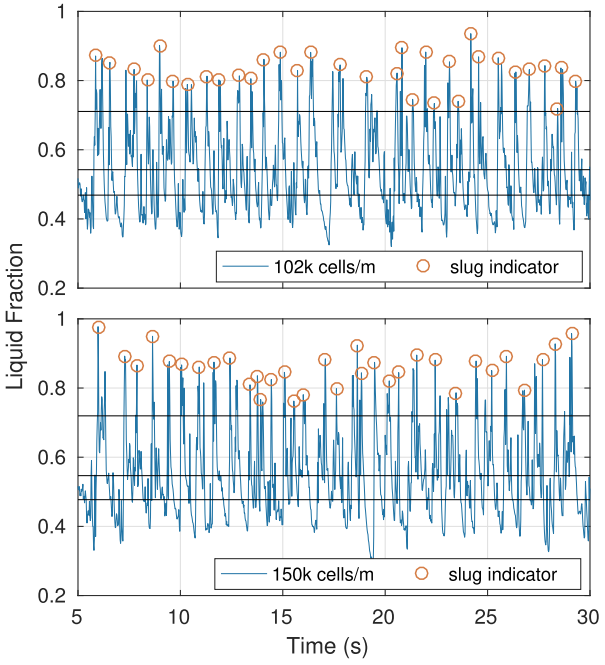

Fig. 5. Holdup profile as a function of time, 7 m pipe 108k cells/m.

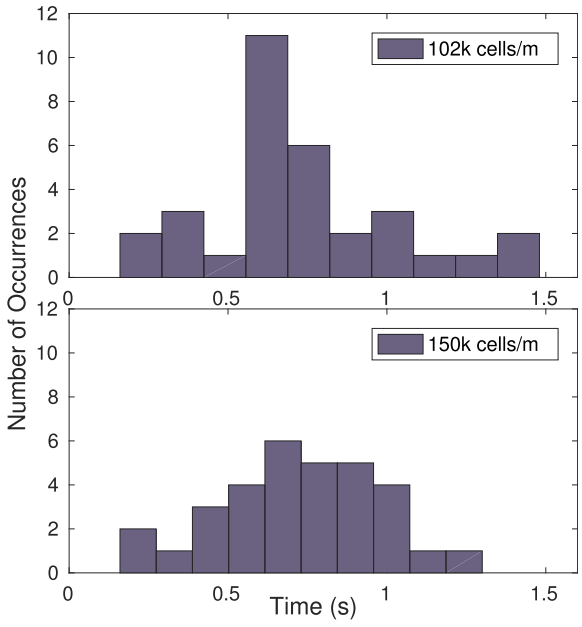

Fig. 6. Histogram of proto slug distribution within 7 m pipe.

The 150k cells/m mesh data spread is reminiscent of a standard distribution. The simulated slug periods ae similar to the experiment data. Most of the data lie between 0.4 and 1.0 s. The experimental mean of 0.697 s is reflected well in both simulations. Although it is possible to calculate a standard deviation, the number of sample points is too low for these simulations to give a meaningful representation of the distribution.

Furthermore, as shown for several of the subsequent cases and the 102k cells/m case, the distribution is not always Gaussian, therefore the standard deviation will not be summarized for the simulations. The mean peak interval is 0.757 s for both cases and match well with the experimental data, to within 10% as summarized in Table 3.

Even though the simulated slug frequency matches well with the experiments ($t = 0.697s$), we notice there are occasional gaps in the simulation data (Fig. 5). These gaps are the result of two proto slugs merging, after the merging there is a long period of time between holdup peaks. A proto slug is a precursor to a slug, often short, that may or may not develop into a stable slug. This merging behavior is most noticeable in the interval between 17 and 20 s of the 102k cells/m mesh (Fig. 5). With additional computational resources it will be possible to ascertain if the phenomenon is related to mesh density. As can be seen from this limited sample the behaviour is diminished in the 150k cells/m mesh.

The merging behaviour is apparent when inspecting a streamwise view of the domain. In Fig. 7, we see the process at which the flow regime quickly develops into two proto slugs from a smooth stratified flow at initialization. The transition from a single slug to two slugs is also clearly demonstrated. The domain appears short in the figure due to doubling the vertical scale for illustration purposes.

At t = 5, 20 and 25 s there is a single visible proto slug, while at t = 10, 15 and 30 s there are two distinct proto slugs at various stages of accumulation. At 10 s, the proto slug structures are depicted in the

Table 3
Summary of proto slug frequency for 7 m pipe.

Cells/m	t (s)	f (Hz)
102 k	0.76	1.32
150 k	0.76	1.32
exp.	0.70	1.43

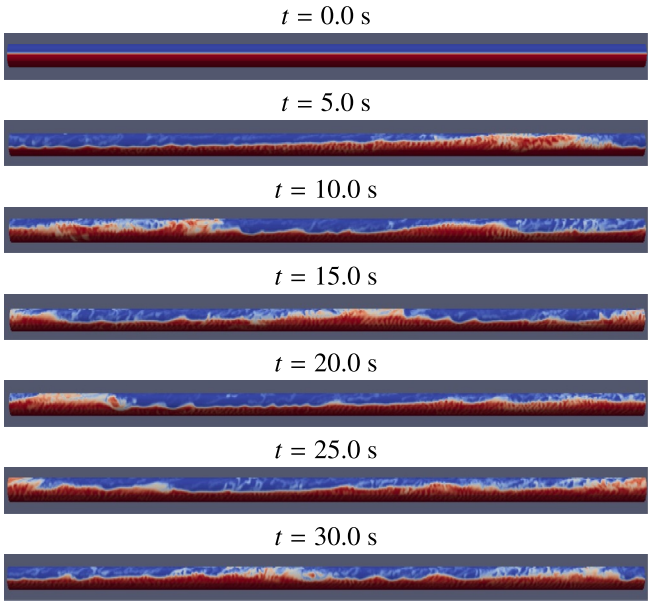

Fig. 7. Snapshots of streamwise phase field.

Fig. 8. Streamwise view of propagating slug.

liquid accumulation stage and nearly occupying the entire cross section at 15 s. Upon observation of the entire time series, the buildup and dissipation of slugs is a reoccurring process. The proto slugs are travelling faster than the waves and thus gathering liquid, which in turn contributes to the growth of the proto slug.

The process during which the liquid body both grows and entraps gas pockets is shown in Fig. 8. The proto slug is absorbing the smaller waves in front. As it absorbs these waves it is accumulating liquid at a faster rate than that which it is depositing liquid at the tail. There is a clear breaking of the front wave which entraps gas and creates gas pockets within the liquid.

If the streamwise cut (Fig. 8) is observed throughout the simulation, there is a noticeable excitation stage in which the proto slug grows and a relaxation period in which it dissipates. During excitation of the flow, the area in front of the accumulation region creates small ripples that grow into waves. The waves merge and create larger waves, and eventually this behavior forms a proto slug. During the dissipation phase, the area in front of the slug calms and the waves die out. This process is repeated and results in a periodic formation and dissipation of proto slugs.

If, instead, we monitor a cross-sectional cut (Fig. 9), it is clear that the bubbles are not dispersed into a swarm of small bubbles within the liquid layer, instead the gas tends to bunch together in large pockets. This contributes to the observed tendency where the liquid layer rarely reaches the top wall. The simulation lacks the resolution to resolve minor bubbles entrapped in the liquid layer. It is likely that this is the root cause of the gas layer we see separating the liquid from the upper wall in Figs. 9 and 7.

The cross section shown in Fig. 9 gives further context to the gas entrapment highlighted in Fig. 8. With further mesh refinement it is likely we would see a more prominent occurrence of small dispersed bubbles.

Although we classify the flow in the experiments as slug flow, this simulation, as well as subsequent meshes and pipe lengths rarely result in the liquid layer completely covering the cross section. This is due to the pockets of gas formed near the top wall. The experimental data gathered by gamma densitometry and visual recordings indicate that the liquid breaches the top wall intermittently, while also creating large gas pockets near the top wall after the slug front. We believe that the discrepancy between experiment and simulation occurs because the mesh is too coarse to resolve small gas bubbles within the liquid layer. The solver obeys the continuity equations and thereby pushes the gas phase toward the top creating large pockets of gas. The replacement of dispersed small bubbles with large gas bubbles will in turn reduce the effective viscosity (Pal, 1996; Pal and Rhodes, 1989; Anisa and Nour, 2010). The combination of the liquid not breaching the top wall and the decreased effective viscosity caused by a lack of small bubbles will lead to an undershoot of the maximum and mean pressure gradient solutions compared to the expected results. Conversely, the minimum values should be representative of the experiments.

Compared to the experiment (Fig. 3), the holdup profile peaks marked in Fig. 5 exist in the region between 80 and 90% holdup, with infrequent peaks above 90%, which is consistent with the 7 and 3 m

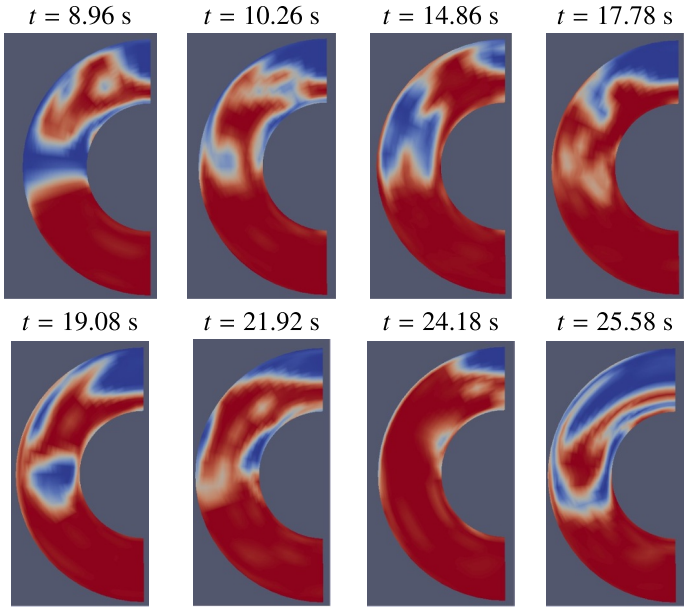

Fig. 9. Snapshots of phase field at selected peaks (Ref. Fig. 5).

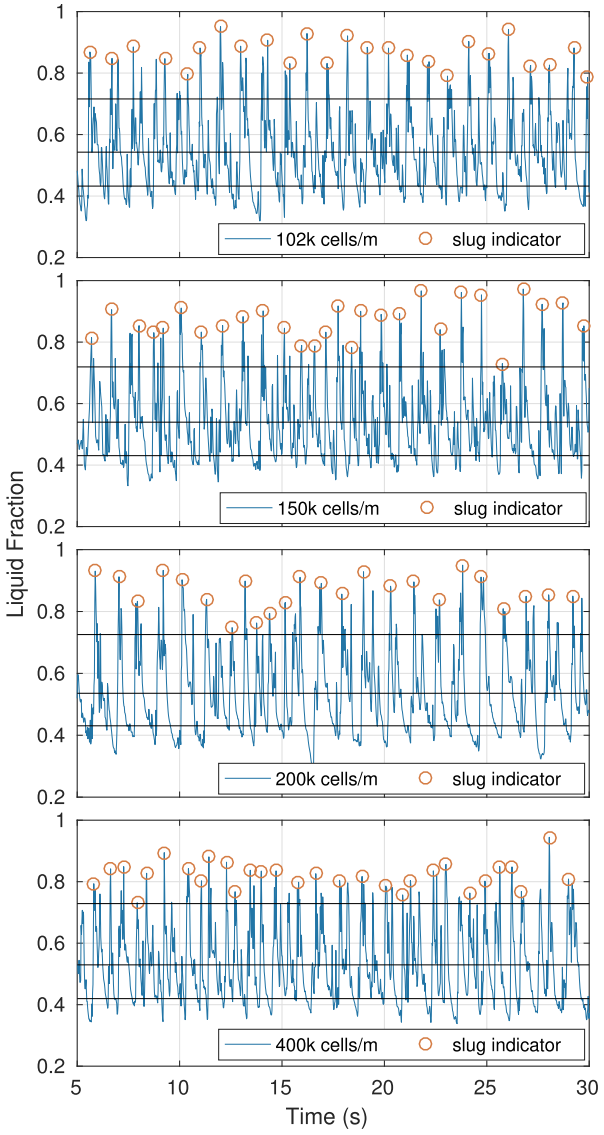

Fig. 10. Holdup profile as a function of time within 5 m pipe.

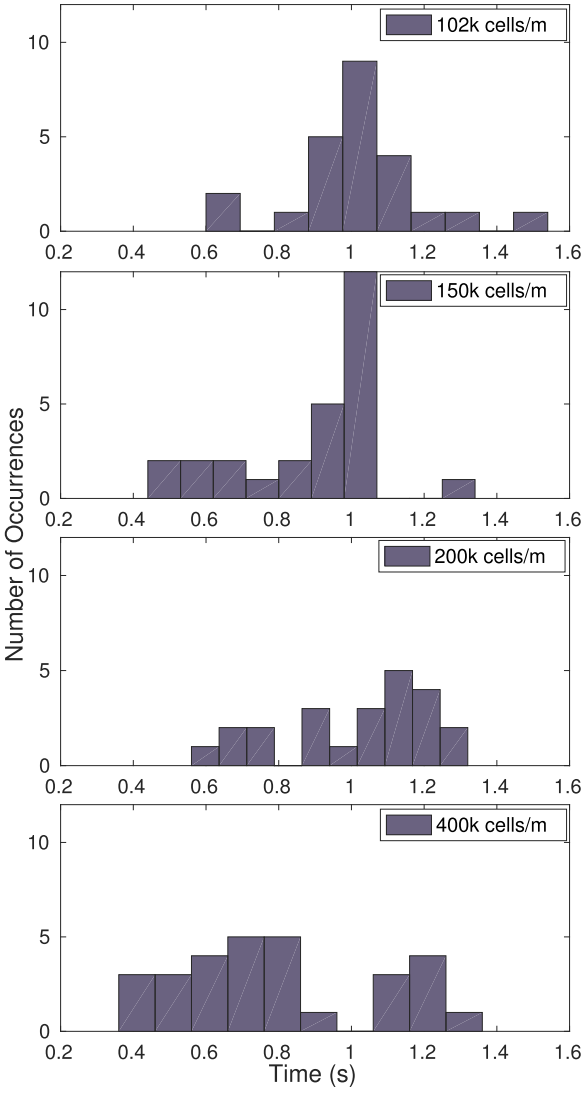

Fig. 11. Histogram of proto slug distribution within 5 m pipe.

simulations (Figs. 10 & 12).

When we compare the holdup profiles as shown in Fig. 10 and the corresponding histograms represented in Fig. 11 with those of the 7 m pipe in Fig. 5 and the experiment (Fig. 3), there is a distinct shift in the proto slug frequency as summarized in Table 4. We notice that, as the mesh is refined, the finer meshes are able to distinguish two slug frequencies. Fig. 10 shows that the two coarse meshes have slug occurrences concentrated around a 1 s interval while the two finer meshes are split between 0.5 and 1.3 s. Concurrent with the mesh refinement there is a distinct shift toward more high frequency slugs and a few low frequency slugs.

As we previously theorized, the 5 m domain is not suitable to accurately represent the slugging frequency of the experiment (1.43 Hz). The flow is likely near the production of persistent secondary proto slugs. As the secondary proto slug merges with the primary and creates one prolonged proto slug, two distinct frequencies are distinguished from the data, as shown in the histograms of the finer meshes (Fig. 11).

The additional liquid available within the domain introduces a strong presence of interfering structures such as waves which were not noted in either the 3 or 7 m simulation. The large waves produced in the 5 m domain are likely caused by the restriction imposed on the simulation by the domain length and initial conditions (I.C). Inspecting the visual data collected at IFE, there does not appear to be any visible large wave structures of this nature in the experiment.

Compared to both the 7 m (Fig. 6) and 3 m domain (Fig. 13) histograms, the statistical representation of the 5 m domain (Fig. 11) indicates a more irregular distribution of the slug period. For the 5 m case, it is apparent that the mesh has a visible effect on the time wise distribution, as shown the center of the most frequent bin(s) shifts from 1 s for the coarser meshes to 0.7 s for the finest mesh. In addition, there is an introduction of additional low frequency occurrences in the range around 1.2 s, a trend which coincides with the mesh refinement.

The overall statistics summarized in Table 4, indicate a reduction of the slugging frequency by 9 to 27% when compared to the 7 m domain, and 16 to 33% reduction compared to the experiment. This result exemplifies that although periodic boundary conditions are often described as simulating an infinite pipe, there are still domain specific artifacts introduced in strong periodic flow such as the slug regime which makes the domain length a critical consideration.

The data collected for the 3 m pipe as represented by Figs. 12 and 13 are statistically summarized in Table 5. They indicate that the frequency of slug occurrences remains relatively stable within a frequency range of 1.36-1.48 Hz, within 5% of the expected behaviour. Visually inspecting the individual mesh solutions (Fig. 12), there are no clear differences in the data sets.

Similarly, as with the 5 and 7 m domains, the vast majority of the

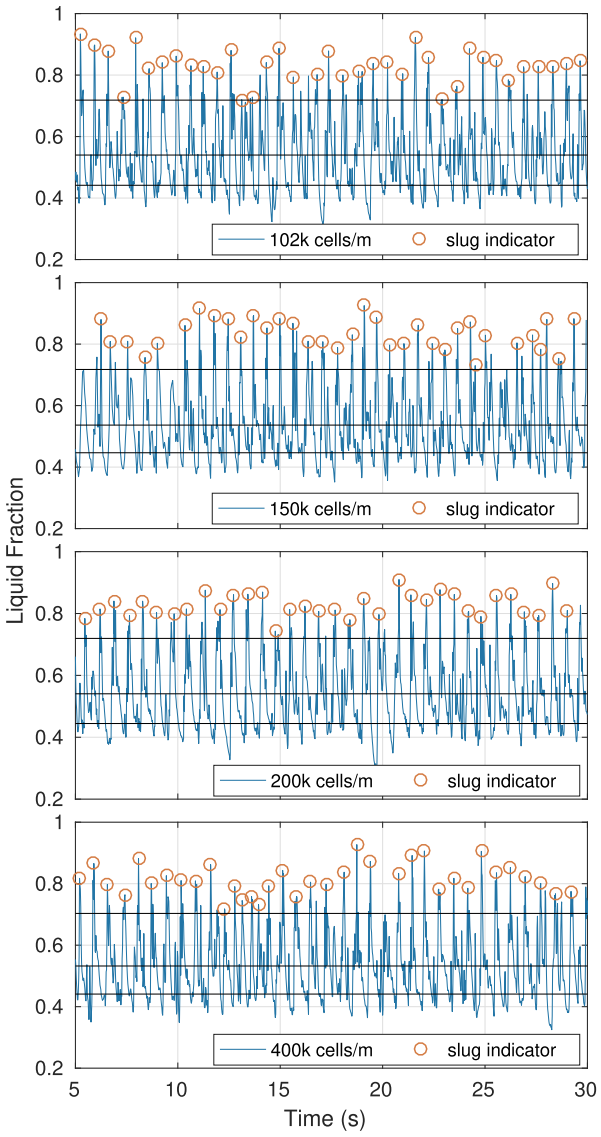

Fig. 12. Holdup profile as a function of time within 3 m pipe.

Table 4
Summary of proto slug frequency for 5 m pipe.

Cells/m	t (s)	f (Hz)
102k	1.00	1.00
150k	0.89	1.12
200k	1.04	0.96
400k	0.83	1.20
exp.	0.70	1.43

slug occurrences exist in the region between 80 and 90% hold up, with some infrequent occurrences above 90%.

The data in Fig. 13 is concentrated for all meshes at the mean interval between 0.68 and 0.74 s (Table 5). When compared to the previous simulations this implies that the short domain imposes a very strong periodic behavior on the flow. As we originally hypothesized, the 5 and 7 m domains both contribute to alleviate this behaviour. For simulation purposes, without very good prior knowledge of the flow conditions it would be complicated to justify such a short domain. The domain has a significant impact on the slug frequency. We see this as the frequency clearly shifts between cases of different length. The 3 and 7 m domain are close to the expected behaviour, these domains were

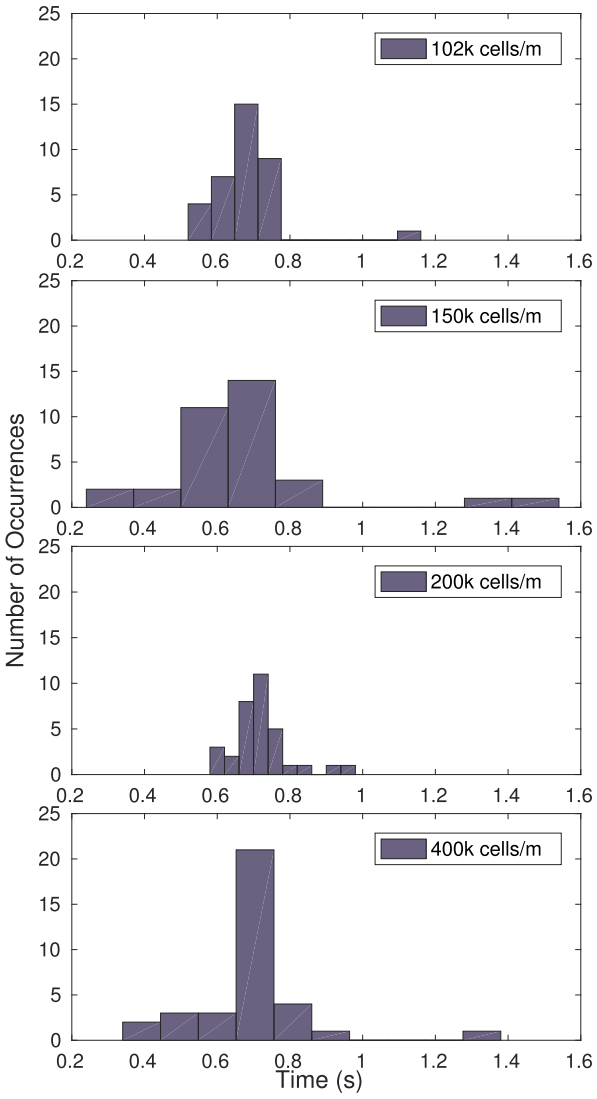

Fig. 13. Histogram of proto slug distribution within 3 m pipe.

Table 5
Summary of proto slug frequency for 3 m pipe.

Cells/m	t (s)	f (Hz)
102 k	0.68	1.48
150 k	0.71	1.40
200 k	0.74	1.36
400 k	0.69	1.44
exp.	0.70	1.43

designed to closely replicate the length between slugs observed in the experiments.

4.2. Measured and simulated pressure gradient results

At IFE the pressure gradient was measured using differential pressure transducers. The data used in this paper was collected 36 and 39 m downstream of the inlet section at a frequency of 1.2 Hz. The pressure gradient data extracted from the simulations was the pressure gradient required to maintain the 3.6 m/s average mixture velocity established during the experiments. The recorded pressure gradient is a correction determined by the solver, as the solver attempts to determine the correction, it takes all the velocity components within the domain into consideration and determines a pressure gradient required to adjust the

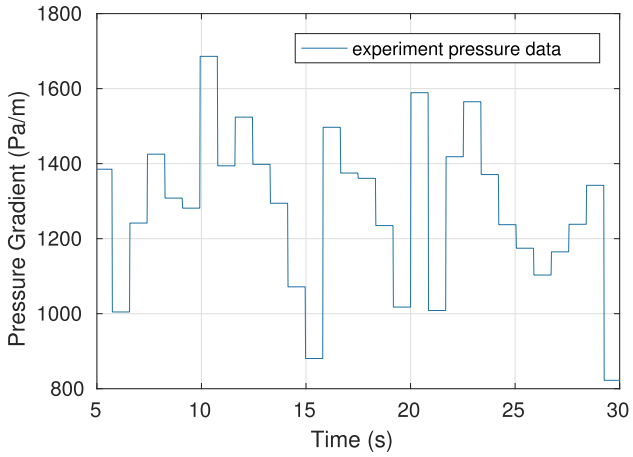

Fig. 14. Experiment pressure gradient as a function of time.

average velocity field of the domain to the set value. Therefore, the pressure gradient is not the differential of 2 points as in the experiments but rather numerically determined as the pressure gradient correction required to maintain the average mixture velocity. For this reason, with regards to the simulations, there is no inherit averaging tied to the length of the domain as could be the case for an experimental case. However, what may have an impact on the pressure gradient, is the number of slugs located within the domain, our hypothesis is as mentioned that the domain length should be close to an integer value of the slug to slug length to minimize the error.

Fig. 14 visualizes a 25 s segment of the experiment pressure gradient as a function of time while Fig. 15 displays the pressure gradient distribution in histogram form. The analysis is performed on the full 100 s data, however for purposes of consistency between experiment and simulation illustrations we only plot a 25 s segment. The periodic buildup of pressure caused by a passing slug and subsequent drop is clearly shown throughout the time lapse in Fig. 14. Keep in mind that due to the low sampling rate (1.2 Hz) it is complicated to compare trends such as frequency of pressure spikes with the simulation data (50 Hz), however maximum, minimum and mean pressure readings will be compared. In addition we will compare threshold data at which 5% of the data is above or below the threshold at both the high and low end of the data. We note that the maximum pressure gradient found in the experiment was 1785 Pa/m while the minimum was 822 Pa/m and the average 1286 Pa/m.

The histogram is used to put further context to the pressure gradient behaviour. The pressure data was originally 5000 data points, however the data collection procedure increases the number of samples artificially to match the holdup data points which results in repeat data.

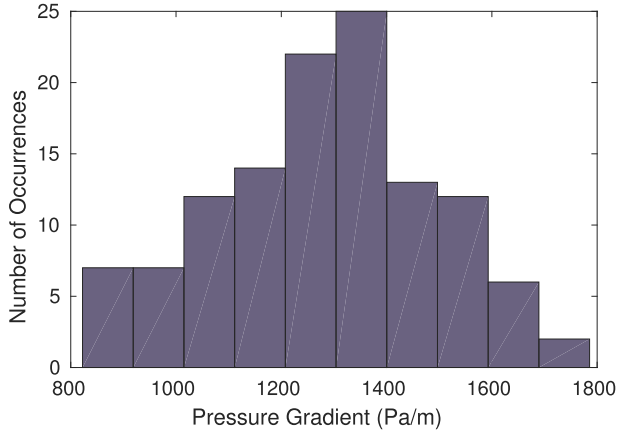

Fig. 15. Experiment pressure gradient histogram.

Therefore the sample is filtered to include each new sample, this reduces the amount of data points to 120. The pressure gradient distribution is centered at 1286 Pa/m and takes a shape resembling a Gaussian distribution.

Instead of using the extreme values for comparison we utilize a threshold at 5% and 95% of the data points to adjust for extreme outliers. These thresholds are the points at each end of the spectrum where 5% of the data is either lower or higher respectively than the threshold value. The 5% threshold is at 880.5 Pa/m while the upper threshold is at 1626.0 Pa/m. Using an upper and lower bound threshold to compare the pressure gradients of the simulations and experiments give a more robust comparison and it is less likely that the point represent an extreme outlier.

In the following sections we will present the pressure solutions for the 7, 5 and 3 m pipe along with the assorted meshes used for each domain length.

4.3. Long pipe (7 m)

Due to the time required to run a simulation for the 7 m domain with finer meshes, the 7 m domain simulation has been restricted to the two coarsest meshes, while remaining domain lengths utilize all 4 meshes.

As with the experiments we notice the oscillating behaviour associated with the buildup and drop off of the pressure gradient as the simulation attempts to maintain the constant average velocity of 3.6 m/s specified as the flow condition.

Similarly to the holdup solutions, we exclude the startup region prior to 5 s for the pressure gradient solution and compare the remaining data with the data gathered in experiment. The maximum and mean pressure gradient values are consistent with those observed in the collected experimental data (Fig. 14) while the minimum pressure gradient deviates significantly from the expected results.

The data summarized in Table 6 indicates that the 150k cells/m mesh performs better with regards to the pressure readings. Overall, the data collected for the two meshes are within 28% of the experiment data. The maximum and mean pressure data are accurately reproduced in the simulations. The relative errors are within 3–8% of the maximum readings and 1% of the mean. while the minimum pressure gradient is significantly higher than expected (19–29%).

In subsequent domains with refined meshes we will notice that typically the pressure gradient values decrease as the mesh is refined.

The extreme values of the experiments and simulations are not necessarily good points of comparison for the statistical behaviour of the flow. Therefore, in addition to the extreme values we utilize thresholds to more robustly evaluate the pressure behaviour.

In order to determine how similarly the solutions are behaving, we analyze the data using a statistical approach (Fig. 17). From this process we can say something about the distribution of the pressure data. The analysis offers a visual representation of both the mean and the extreme values at a glance. The data is summarized in Table 7 and shows that this approach, although still deviatory compared to the experiments, conforms to the trends noticed in the extreme value comparison.

The results summarized in Table 7 exemplifies a difference between the simulations and the experiments which is not readily available by looking at the max and minimum values as shown in Table 6. Although the general behaviour is consistent with the extreme values when using

Table 6
Summary of pressure gradient data for the 7 m pipe.

Cells/m	Mean (Pa/m)	Max (Pa/m)	Min (Pa/m)
102k	1295.4	1641.7	1058.2
150k	1299.7	1735.3	980.9
exp.	1286.0	1785.0	822.0

Table 7
Summary of pressure gradient histogram data for the 7 m pipe.

Cells/m	Mean (Pa/m)	95% (Pa/m)	5% (Pa/m)
102k	1295.4	1493.8	1127.3
150k	1299.7	1503.7	1114.8
exp.	1286.0	1626.4	880.5

a 5% threshold, it is clear that the bulk of the low and high pressure gradient results are closer to the mean, which results in a slightly larger gap than that seen from merely comparing the extreme values. Utilizing an approach which builds on a percentage of data points instead of extreme values gives a clearer picture of how the simulation pressure solutions are behaving compared to the experiments. The largest errors which are associated with the lower bounds are within 30% of the expected results, while the mean and upper bounds relative errors are significantly smaller, at approximately 1% and 8% respectively.

4.4. Medium pipe (5 m)

The 5 m pipe simulation results in a lower slugging frequency than the 3 and 7 m pipes but is still expected to exhibit similar trends with regards to the mean pressure gradient. In addition we would expect to see a prolonged pressure trough in the region between 25 and 27 s where the noted holdup drop was for the 150k cells/m mesh (Fig. 10).

Referencing Table 8 we notice a negative shift of the maximum, min and mean pressure gradient values from the 102 to 200k cells/m mesh solutions. The finest mesh has a minor pressure gradient increase when compared to the 200k cells/m mesh, for all recorded parameters. The trends hold true for both the extreme values (Table 8 and the threshold values (Table 9).

The extreme values are as mentioned not necessarily accurate representations as they could in some cases be an extreme outlier, for that reason we plot the data as histograms and find the 5 percentile threshold at either end of the spectrum.

The statistical representation of the pressure gradient solution shown in Fig. 19 clearly indicate that the mean values of the solution shift toward a lower value as the mesh density increases. We also notice that the front tail of the distribution closely follows a normal distribution pattern. The back tail of the histogram is cut short for the finer meshes. These types of distributions resemble a positive skew normal distribution. The behaviour is also present in the 3 m domain. By sorting the data in ascending order and choosing the 5 percentile data points at either tail of the data we can determine a more representative threshold for the high and low pressure boundaries, these thresholds are summarized in Table 9.

With regards to mesh dependency, there is no great difference between the relative errors of the mean,max and minimum pressure gradient data for the two finer meshes. However, there is significant discrepancy between the min and max relative errors with respect to the experiments as shown in Fig. 20 and Table 9. This particular case has a reduced slugging frequency due to restriction of available liquid tied to the length of the domain, which in turn will have an impact on the pressure solution. The solutions tend to stabilize as the mesh is refined and the gap between mean and extreme values stays relatively

Table 8
Summary of pressure gradient information for the 5 m pipe.

Cells/m	Mean (Pa/m)	Max (Pa/m)	Min (Pa/m)
102k	1316.7	1776.5	1023.4
150k	1276.0	1733.5	965.5
200k	1051.0	1448.0	840.2
400k	1069	1515.8	865.0
exp.	1286.0	1785.0	822.0

Table 9
Summary of pressure gradient information for the 5 m pipe.

Cells/m	Mean (Pa/m)	95% (Pa/m)	5% (Pa/m)
102k	1316.7	1495.6	1147.7
150k	1276.1	1518.6	1042.1
200k	1065.5	1267.7	910.8
400k	1074.0	1277.1	910.8
exp.	1286.0	1626.4	880.5

constant. We can conclude that for this domain length and slugging frequency the solution consistently undershoots the mean and maximum pressure gradients (Table 8). This could be a direct result of the reduced slugging frequency (Table 4) as it is the slugs that introduce the large pressure spikes.

There is a large pressure gradient drop of approximately 250 Pa/m from the 102k cells/m mesh to the 200k cells/m mesh, after which the solution stabilizes. A probable cause for this phenomenon is that the coarser meshes are not resolving some of the finer structures within the pipe. Surprisingly, the coarsest mesh is closest to the experiment results for the mean and minimum values. However, remember that this particular domain size does not accurately replicate the experimental slug frequency as seen in Table 4. As such, neither mesh is expected to give a particularly good replication of the experiment.

Overall, apart from the 102k cells/m mesh, the results were within 21.5% relative error with respect to the experiments.

4.5. Short pipe (3 m)

In the following figures and tables, we will compare the 3 m domain pressure behavior (Fig. 21) with that seen within the 5 and 7 m domains (Figs. 18 & 16) as well as experiment results.

Comparing the different meshes of the 3 m domain in Fig. 21, there are a few noticeable differences. Foremost, it is evident that the mean pressure gradient decreases as the mesh count increases (Table 10), which is consistent with the 5 m case (Table 8). The mean pressure gradient of the 102k and 150k cells/m mesh are and 1205.7 and 1263.6 Pa/m respectively. Comparatively the two finer meshes are 1065.5 and 1074 (Table 10).

Beyond the first 10 s the location of the minimums and maximum

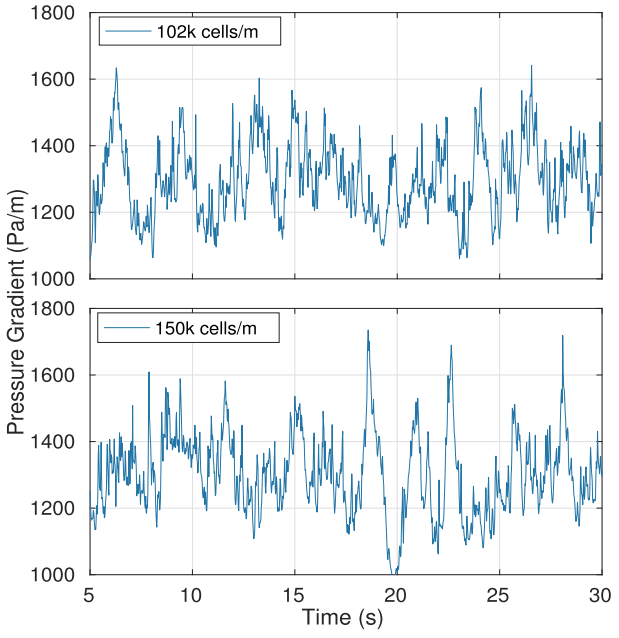

Fig. 16. Pressure gradient as a function of time, 7 m pipe 108k cells/m.

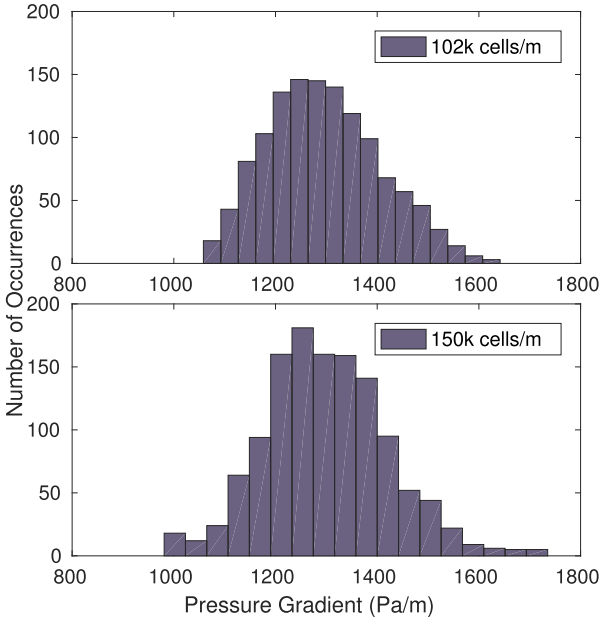

Fig. 17. Pressure gradient histogram, 7 m pipe.

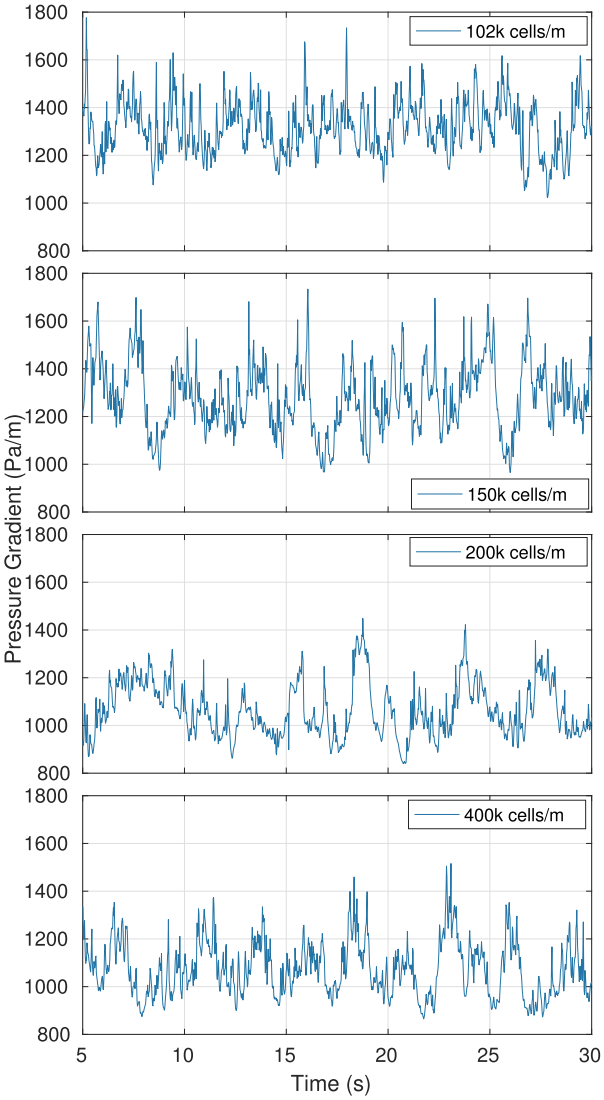

Fig. 18. Pressure gradient as function of time 5 m pipe.

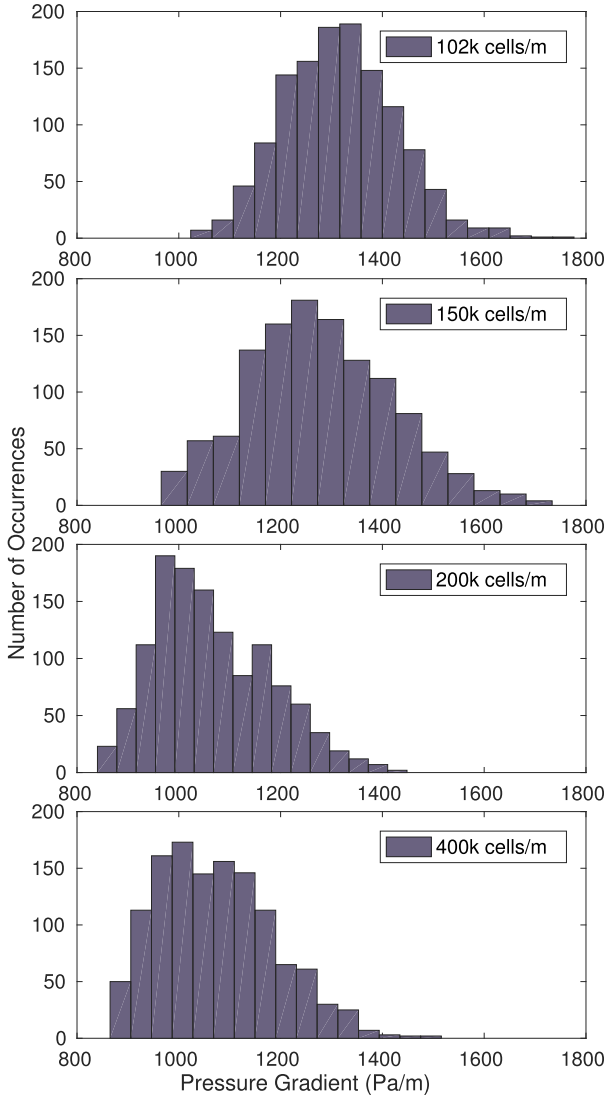

Fig. 19. Pressure gradient histogram, 5 m pipe.

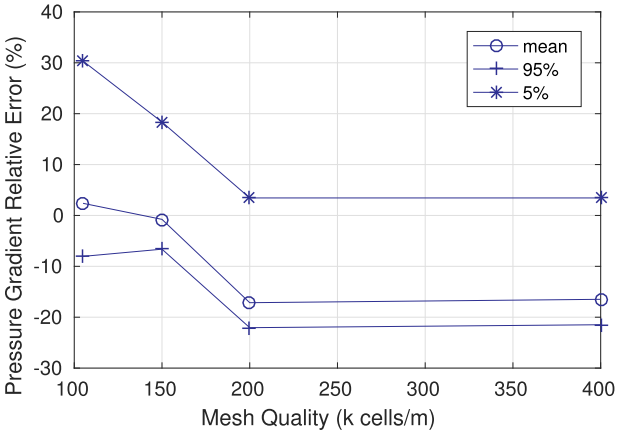

Fig. 20. Pressure gradient relative error as a function of cell count.

peaks are nearly synchronized in time as seen at the peak on either side of the 20 s mark. Also note that the maximum value (2241 Pa/m) recorded for the 150 k cells/m mesh is 400 Pa/m higher than any data point prior to it. If we were to exclude this data point, the maximum value would be in line with the trend of the remaining meshes as shown in Table 10.

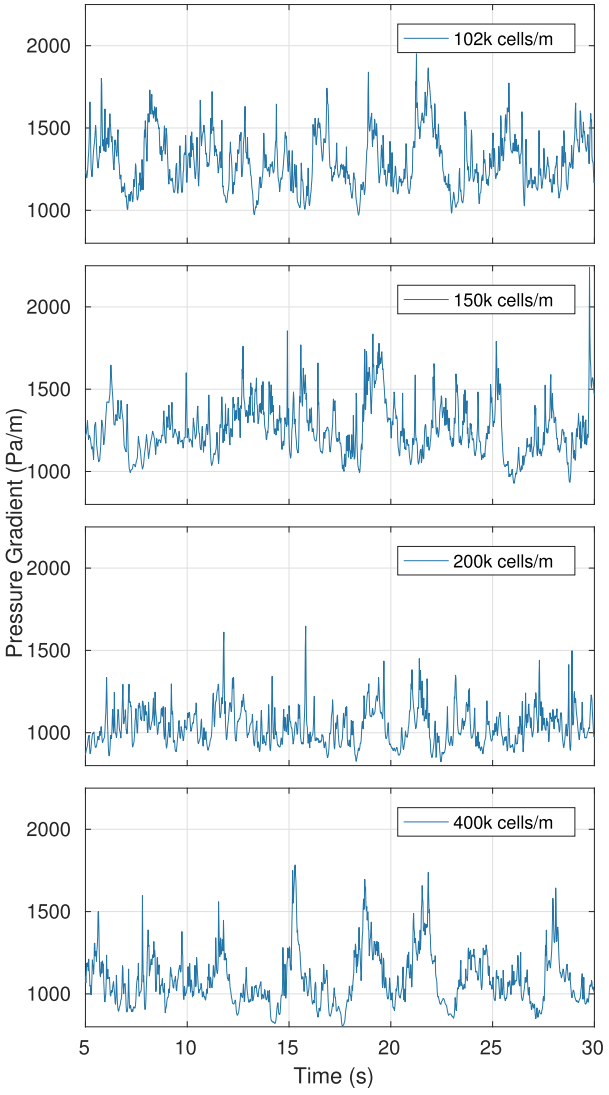

Fig. 21. Pressure gradient as a function of time within 3 m pipe.

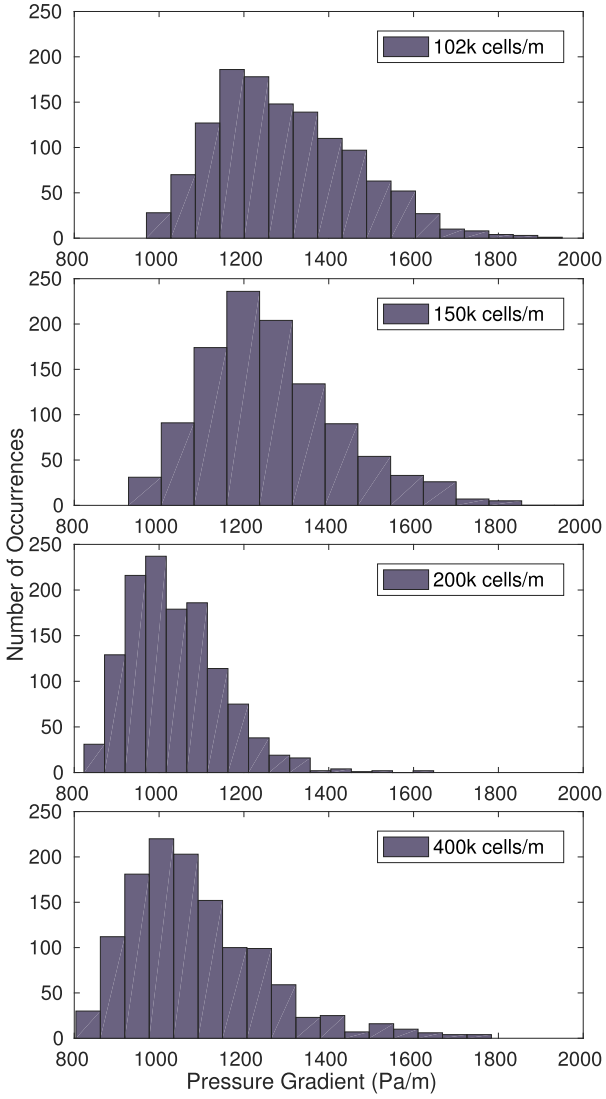

Fig. 22. Pressure gradient histogram, 3 m pipe.

Table 10
Summary of pressure gradient information for the 3 m pipe.

Cells/m	Mean (Pa/m)	Max (Pa/m)	Min (Pa/m)
102k	1295.7	1950.5	970.2
150k	1263.6	2241.1	927.9
200k	1037.5	1647.3	822.9
400k	1087.2	1783.5	803.9
exp.	1286.0	1785.0	822.0

From Table 10 we observe that the pressure gradient of the 3 m domain has undergone a shift when compared to the 5 m domain (Table 8). All the maximum pressure readings have increased and the minimum decreased. The maximum pressure gradient determined during the simulation of the finest mesh was 1783.5 Pa/m at 15.3 s. This is an excellent match to the experimentally determined maximum of 1785 Pa/m. Similarly, the minimal gradient observed in the simulations was 2.2% lower than the experimental value and was 803.9 Pa/m. The mean pressure gradient was lower than expected and averaged out to 1087 Pa/m which is 15.5% lower than the experimental value of 1286 Pa/m. This behavior is consistently noted throughout all domains.

The pressure gradient data shown in Fig. 22 indicates that all the 3 m solutions are resembling a positive skew normal distribution. The front tail seemingly closely follows a Gaussian distribution, however the back tail is cut short. Additionally, the histograms provide a visual representation of how the mean pressure gradient shifts towards a lower value as the mesh is refined. As with prior cases, we will sort the data and indicate an upper and lower 5% pressure threshold to adjust for extreme outliers.

As summarized in Table 11, the general trends noted from preceding cases holds true for the threshold data. As the mesh is refined the pressure gradients decrease. We suggest that the reason why the pressure solutions tend to undershoot is that there is a lack of dispersed small bubbles through the liquid layer. The gas bubbles formed are large and as a byproduct of conservation laws and buoyancy they tend to be pushed to the top, which hinders the formation of conventional slugs. The effect of this behavior on the pressure gradient would be twofold, not only would it reduce the effective viscosity, but also it

Table 11
Summary of pressure gradient information for the 3 m pipe.

Cells/m	Mean (Pa/m)	95% (Pa/m)	5% (Pa/m)
102k	1295.7	1589.8	1054.2
150k	1263.6	1574.3	1034.2
200k	1037.5	1231.4	890.5
400k	1087.2	1392.5	878.9
exp.	1286.0	1626.4	880.5

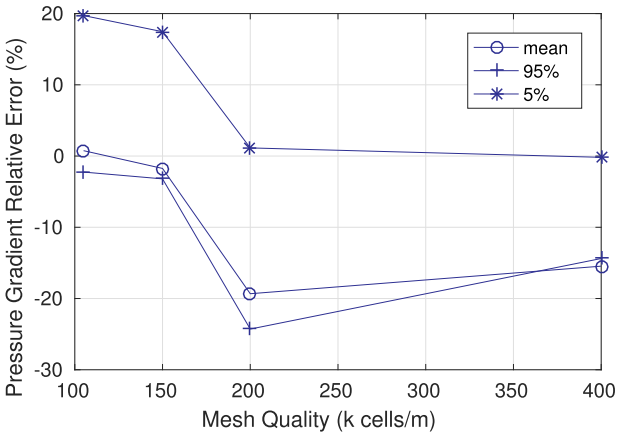

Fig. 23. Pressure gradient relative error as a function of cell count.

would reduce the pressure gradients as the liquid layer does not cover the cross section. Such behavior would most easily be noticed in the high pressure and mean pressure gradient readings while the minimum values should remain consistent with the experiments.

In the following figure we show that the relative error is a better match to the experimental values (Fig. 23) than what was observed in the 5 m mesh (Fig. 20).

The relative errors for the 3 m pipe show the same general trends as the 5 m pipe in terms of refinement behavior. The 150k cells/m mesh undershoot the maximum values by a marginal amount while dropping for the two finer meshes. There is a small improvement from the medium to the finest mesh for all 3 parameters, and overall the errors related to the 3 m case are smaller than those of the 5 m case

For the 3 m domain the best reproduction of experiment results are achieved by the 400k cells/m mesh. When comparing the results with the 5 m domain, we see that they both undershoot the mean value by approximately 15%, while the max and min values are better represented in the 3 m domain. This is an expected result because the 3 m domain closely replicates the distance between slugs. The finest mesh is within 15.5% error for all the recorded values.

Unfortunately, the 7 m case does not have a 200 nor a 400k cells/m simulation, as it would be interesting to compare the pressure solutions for the finest meshes of each case.

5. Conclusion

A series of simulations were run using OpenFOAM and the built in VOF type solver interFoam. The simulations were run using 3, 5 and 7 m long domains employing a concentric annulus configuration. The outer and inner diameters were 0.1 and 0.05 m respectively. The meshes varied from 102k cells/m to 400k cells/m. Due to the impact of mesh density on simulation time, the 7 m domain was only run with the 2 coarsest meshes. The data was analyzed with respect to pressure gradient and holdup profile and compared to experimental data.

During the course of these simulations we noticed a significant impact of the domain length on the slug frequency as well as on the pressure distribution. For both of the 3 m and 7 m domains, the simulation results compare favourably with the experimental data. As the mesh density increases there is a clear trend that the minimum and maximum pressure gradient values converge toward the experimental values of 1785 and 822 Pa/m respectively, the threshold data also show some signs of convergence however there is a larger gap for the maximum and mean data. The 3 m domain with a fine mesh maintained the 5% threshold minimum relative error to within 3% while the mean and max relative error were below 15.5%. For all cases the largest error associated with any of the extreme values or mean was within 30% including the outlier case of the 5 m pipe.

The simulation of the 3 m domain with a 400k cells/m mesh gave minimum, mean and maximum values of 803, 1074 and 1783.5 Pa/m respectively. Compared to the experimentally measured 822, 1286 and 1785 Pa/m, the extreme values are within 3% of the expected results. In general the simulations are better at predicting minimum values for the finer meshes than they are at predicting maximum mean values. A persistent trend is that as the mesh density is increased, the pressure gradients decrease. A likely reason the maximum and mean pressure gradients undershoot the expected results is that the proto slugs seen in the simulations rarely breach the top wall, in addition the lack of small bubbles within the liquid layer reduces the effective viscosity of the mixture. This effect would be much less prevalent in the minimum pressure gradient results as these readings would not be associated with proto slugs.

The slugging frequencies determined from the 3 m and 7 m domains are representative of the experiments in the sense that the slugging frequency lies within an error margin of 8% of the experiments. The 7 m domain results in a slugging frequency of 1.32 Hz, while the 3 m domain slug frequency lies within a range between 1.36 and 1.48 Hz depending on the mesh. For comparison, the experiments produced slugs at an average frequency of 1.43 Hz. This supports the initial hypothesis that slug flow in a concentric annulus can be studied using a computational representation of the experiments.

The 5 m domain, which is not long enough to include two slugs, did not reproduce the slug frequency nor the minimum or maximum pressure gradients measured in experiment. The result is that we observe large errors in at least 1 extreme value for each mesh for the 5 m domain as well as significant deviation in slug frequency between meshes and experiment result.

Based on the comparison between experimental and simulation data, in order to accurately replicate experimental data using periodic boundary conditions for a flow of a periodic nature such as slug flow, the of the domain must be considered. The computational domain should be approximately equal to an integer number of slug units (distance between two slug fronts or tails). In the case where the domain length is between 1 and 2 slug units such as the 5 m long domain, the slug frequency and pressure distribution will be imposed with an artificial restraint and not be an accurate representation of the physical domain.

We determined that for the sake of reproducing slug frequencies and pressure gradients within an annulus configuration, simulations are accurately able to represent the behavior within a physical pipe. Close attention is required when designing a simulation using periodic boundary conditions, as there are artificial restraints imposed on the simulation also by the initial conditions. In an ideal simulation, a much longer domain would be utilized, such that several slugs can form within the domain simultaneously. This would provide the best representation of a physical domain. However, with the computational demands such a simulation requires, we have attempted to simplify the simulations by using shorter domains and periodic boundary conditions. With this approach some information is needed on the physical flow conditions prior to attempting an accurate simulation.

As shown in the 5 m domain, large discrepancies are introduced when the computational domain is not representative of the experiment. In short, this means that simulations which utilize periodic boundary conditions are unlikely to be fully predictive unless they are also utilizing long domains accompanied with some prior knowledge of the flow conditions. Utilizing a very long domain comes with its own drawback of prohibitive simulation times. To counteract the computational demands related to a longer domain, we have attempted to accurately replicated experiment data using short domains accompanied with detailed knowledge of physical flow conditions.

Potential topics for future studies which are not covered in the current work are the effects of phase fractions, eccentricity, and fluid properties on the resulting flow pattern and characteristics. Each of these present challenging topics with the potential to drastically alter the resulting flow regime.

Acknowledgements

This work is part of a larger project called Multiphase Flow in Concentric and Eccentric Annulus Spaces (project number 255481) and has been performed thanks to funding from the Research Council of Norway through the PETROMAKS2 programme.

References

Anisa, A.I., Nour, A., 2010. Affect of viscosity and droplet diameter on water-in-oil (w/o) emulsions: an experimental study. Int. J. Chem. Mol.Eng. 4, 213–216.
Bellarby, J., Kofoed, S., Marketz, F., 2013. Annular pressure build-up analysis and methodology with examples from multifrac horizontal wells and hpht. SPEI/IADX Drilling Conference. Society of Petroleum Engineers, Amsterdam, Netherlands. https://doi.org/10.2118/163557-MS.
Berberovic, E., 2010. Investigation of Free-surface Flow Associated with Drop Impact: Numerical Simulations and Theoretical Modeling. TU Darmstadt Ph.D. thesis.
Bicalho, I., dos Santos, D., Ataíde, C., Duarte, C., 2016. Fluid-dynamic behavior of flow in partially obstructed concentric and eccentric annuli with orbital motion. Int. J. Heat Fluid Flow 137, 202–213. https://doi.org/10.1016/j.petrol.2015.11.029.
BP, 2010. Deepwater Horizon Accident Investigation Report. Technical Report.
Caetano, E., 1985. Upward Vertical Two-Phase Flow Through an Annulus. The University of Tulsa.
Chung, S., Sung, H., 2003. Direct numerical simulation of turbulent concentric annular pipe flow part 2: heat transfer. Int. J. Heat Fluid Flow 24, 399–411. https://doi.org/10.1016/S0142-727X(03)00017-1.
Chung, S., Sung, H., 2005. Large-eddy simulation of turbulent flow in a concentric annulus with rotation of an inner cylinder. Int. J. Heat Fluid Flow 26, 191–203. https://doi.org/10.1016/j.ijheatfluidflow.2004.08.006.
Colombo, M., Fairweather, M., 2015. Multiphase turbulence in bubbly flows: Rans simuilations. Int. J. Multiphase Flow 77, 222–243. https://doi.org/10.1016/j.ijmultiphaseflow.2015.09.003.
Deshpande, S., Anumolu, L., Trujillo, M., 2012. Evaluating the performance of the two-phase flow solver interfoam. Comput. Sci. Discovery 5, 47–55. https://doi.org/10.1088/1749-4699/5/1/014016.
Dianat, M., Skarysz, M., Garmory, A., 2017. A coupled level set and volume of fluid method for automotive exterior water management applications. Int. J. Multiphase Flow 91. https://doi.org/10.1016/j.ijmultiphaseflow.2017.01.008.
Ekberg, N., Ghiaasiaan, S., Abdel-Khalik, S., Yoda, M., Jeter, S., 1999. Gas-liquid two-phase flow in narrow horizontal annuli. Nucl. Eng. Des. 192, 59–80. https://doi.org/10.1016/S0029-5493(99)00078-3.
Escudier, M., Gouldson, I., Oliveira, P., Pinho, F., 2000. Eects of inner cylinder rotation on laminar ow of a newtonian ïuid through an eccentric annulus. Int. J. Heat Fluid Flow 21, 92–103. https://doi.org/10.1016/S0142-727X(99)00059-4.
Frank, T., 2005. Numerical simulation of slug flow regime for an air-water two-phase flow in horizontal pipes. The 11th International Topical Meeting on Nuclear Reactor Thermal-Hydraulics. Avignon, France
Gidaspow, D., Li, F., Huang, J., 2013. A cfd simulator for multiphase flow in reservoirs and pipes. Powder Technol. 242, 2–12. https://doi.org/10.1016/j.powtec.2013.01.047.
Hadžiabdić, M., Hanjalić, K., Mullyadzhanov, R., 2013. Les of turbulent flow in a concentric annulus with rotating outer wall. Int. J. Heat Fluid Flow 43, 74–84. https://doi.org/10.1016/j.ijheatfluidflow.2013.05.008.
Hasan, A., Kabir, C., 1992. Two-phase flow in vertical and inclined annuli. Int. J. Multiphase Flow 18, 279–293. https://doi.org/10.1016/0301-9322(92)90089-Y.
Hossain, A., Naser, J., Imteaz, M., 2011. Cfd investigation of particle deposition in a horizontal looped turbulent pipe flow. Environ. Model. Assess. 16, 359–367. https://doi.org/10.1007/s10666-011-9252-8.
Housz, E.I., Ooms, G., Henkes, R., Porquie, M., Kidess, A., Radhakrishnan, R., 2017. A comparison between numerical predictions and experimental results for horizontal core-annular flow with a turbulent annulus. Int. J. Multiphase Flow 95, 271–282. https://doi.org/10.1016/j.ijmultiphaseflow.2017.01.020.
Hua, J., Nordbø, J., Foss, M., 2014. Cfd modelling of gas entrainment at a propagating slug front. Proceedings of the 10th international Conference on CFD in Oil and Gas, Metallurgical and Process Industries. Sintef Proceedings, Trondheim, Norway.
Issa, R., Kempf, M., 2003. Simulation of slug flow in horizontal and nearly horizontal pipes with the two fluid-model. Int. J. Multiphase Flow 29, 69–95. https://doi.org/10.1016/S0301-9322(02)00127-1.
Jeong, J., Ozar, B., Dixit, A., Juliá, J., Hibiki, T., Ishii, M., 2008. Interfacial area transport of vertical upward air-water two-phase flow in an annulus channel. Int. J. Heat Fluid Flow 29, 178–193. https://doi.org/10.1016/j.ijheauitow.2007.07.00.
Julia, J., Hibiki, T., 2011. Flow regime transition criteria for two-phase flow in a vertical annulus. Int. J. Heat Fluid Flow 32, 993–1004. https://doi.org/10.1016/j.ijheatfluidflow.2011.06.001.
Julia, J., Ozar, B., Jeong, J., Hibiki, T., Ishii, M., 2011. Flow regime development analysis in adiabatic upward two-phase flow in a vertical annulus. Int. J. Heat Fluid Flow 32, 164–175. https://doi.org/10.1016/j.ijheatfluidflow.2010.09.003.
Kelessidis, V., Dukler, A., 1989. Modeling flow pattern transitions for upward gas-liquid flow in vertical concentric and eccentric annuli. Int. J. Multiphase Flow 15, 173–191. https://doi.org/10.1016/0301-9322(89)90069-4.
Khalili, M., Yahyazadeh, H., Gorji-Bandpy, M., Ganji, D., 2016. Application of volume of fluid method for simulation of a droplet impacting a fiber. Propul. Power Res. 5, 122–123. https://doi.org/10.1016/j.jppr.2016.04.003.
Knotek, S., 2014. Numerical simulation of multiphase flows in large horizontal pipes. Proceedings of the 17th International Flow Measurement Conference FLOMEKO 2016. International Measurement Confederation, Taipei, Taiwan.
Lopes, P., 2013. Free-surface Flow Interface and Air-Entrainment Modelling Using OpenFOAM. University of Coimbra:Department of Civil Engineering.
LP, E. S., 2014. Deepwater Horizon Blowout Preventer Failure Analysis Report.
Nuland, S., 1999. Bubble fraction in slugs in two-phase flow with high viscosity liquid. Proceedings of the 2nd International Symposium on Two-phase Flow Modeling and Experimentation. https://doi.org/10.1088/1757-899X/121/1/012018. Pisa, Italy
Pal, R., 1996. Effect of droplet size on the rheology of emulsions. Am. Inst. Chem. Eng. 42, 3181–3190. https://doi.org/10.1002/aic.690421119.
Pal, R., Rhodes, E., 1989. Viscosity/concentration relationships for emulsions. J. Rheol. 33, 1021–1045. https://doi.org/10.1122/1.550044.
Parsi, M., Azzopardi, B., Al-Sarkhi, A., Kesana, N., Vieira, R., Torres, C., McLaury, B., Shirazi, S., Schleicher, E., Hampel, U., 2017. Do huge waves exist in horizontal gas-liquid pipe flow? Int. J. Multiphase Flow 96, 1–23. https://doi.org/10.1016/j.ijmultiphaseflow.2017.06.007.
Pietrzak, M., Witczak, S., 2013. Flow patterns and void fractions of phases during gas-liquid two-phase and gas-liquid-liquid three-phase flow in u-bends. Int. J. Heat Fluid Flow 44, 700–710. https://doi.org/10.1016/j.ijheatfluidflow.2013.09.007.
Rzehak, R., Krepper, E., 2013. Cfd modeling of bubble-induced turbulence. Int. J. Multiphase Flow 55, 138–155. https://doi.org/10.1016/j.ijmultiphaseflow.2013.04.007.
Rzehak, R., Kriebitzsch, S., 2015. Multiphase cfd-simulation of bubbly pipe flow: a code comparison. Int. J. Multiphase Flow 68, 135–152. https://doi.org/10.1016/j.ijmultiphaseflow.2014.09.005.
Shuard, A., Mahmud, H., King, A., 2016. Comparison of two-phase pipe flow in openfoam with a mechanistic model. Proceedings of the IOP Conference Series: Materials Science and Engineering Volume 121. IOP Publishing Ltd, Trondheim, Norway. https://doi.org/10.1088/1757-899X/121/1/012018.
So, K., Hu, X., Adams, N., 2011. Anti-diffusion method for interface steepening in two-phase incompressible flow. J. Comput. Phys. 230, 5155–5177. https://doi.org/10.1016/j.jcp.2011.03.011.
Sorgun, M., Osgouei, R., Ozbayoglu, M., Ozbayoglu, A., 2013. An experimental and numerical study of two-phase flow in horizontal eccentric annuli. Energy Sources Part A 35, 891–899. https://doi.org/10.1080/15567036.2011.559524.
Taitel, Y., Dukler, A., 1976. A model for predicting flow regime transitions in horizontal and near horizontal gas-liquid flow. Am. Inst. Chem. Eng. 22, 47–55. https://doi.org/10.1002/aic.690220105.
Transocean, 2011. Macondo Well Incident.
Tunstall, R., Skillen, A., 2016. Large eddy simulation of a t-junction with upstream elbow: the role of dean vortices in thermal fatigue. Appl. Therm. Eng. 107, 672–680. https://doi.org/10.1016/j.applthermaleng.2016.07.011.
Ubbink, O., 1997. Numerical Prediction of Two Fluid Systems with Sharp Interfaces. Imperial College.
Valle, C., Hohne, T., Prasser, H., Shnel, T., 2008. Experimental investigation and cfd simulation of horizontal stratified two-phase flow phenomena. Nucl. Eng. Des. 238, 637–646. https://doi.org/10.1016/j.nucengdes.2007.02.051.
Verdin, P., Thompson, C., Brown, L., 2014. Cfd modelling of stratified/atomization gas-liquid flow in large diameter pipes. Int. J. Multiphase Flow 67, 135–143. https://doi.org/10.1016/j.ijmultiphaseflow.2014.07.008.
Weller, G., 2008. A New Approach to VOF-based Interface Capturing Methods for Incompressible and Compressible Flow. Technical Report.
Wongwises, S., Pipathattakul, M., 2006. Flow pattern, pressure drop and void fraction of two-phase gas-liquid flow in an inclined narrow annular channel. Exp. Therm. Fluid Sci. 30, 345–354. https://doi.org/10.1016/j.expthermflusci.2005.08.002.
Xiang, M., Cheung, S., Yeoh, G., Zhang, W., Tu, J., 2011. On the numerical study of bubbly flow created by ventilated cavity in vertical pipe. Int. J. Multiphase Flow 37, 756–768. https://doi.org/10.1016/j.ijmultiphaseflow.2011.01.014.
Xin, R., Awwad, A., Dong, Z., Ebadian, M., 1997. An experimental study of single-phase and two-phase flow pressure drop in annular helicoidal pipes. Int. J. Heat Fluid Flow 18, 482–488. https://doi.org/10.1016/S0142-727X(97)80006-9.
Xing, L., Yeung, H., Shen, J., Cao, Y., 2013. Numerical study on mitigating severe slugging in pipeline/riser system with wavy pipe. Int. J. Multiphase Flow 53, 1–10. https://doi.org/10.1016/j.ijmultiphaseflow.2013.01.003.
Zambrano, H., Sigalotti, L., Klapp, J., Polo, F., Bencomo, A., 2017. Heavy oil slurry transporation through horizontal pipelines: experiments and cfd simulations. Int. J. Multiphase Flow 91, 130–141. https://doi.org/10.1016/j.ijmultiphaseflow.2016.04.013.